The sensitivity of estimates of multiphase fluid and solid properties of porous rocks to image processing

Gaetano Garfi · Cédric M. John · Steffen Berg · Samuel Krevor

Received: date / Accepted: date

Abstract X-ray microcomputed tomography (X-ray μ-CT) is a rapidly advancing technology that has been successfully employed to study flow phenomena in porous media. It offers an alternative approach to core scale experiments for the estimation of traditional petrophysical properties such as porosity and single-phase flow permeability. It can also be used to investigate properties that control multi-phase flow such as rock wettability or mineral topology. In most applications, analysis are performed on segmented images obtained employing a specific processing pipeline on the greyscale images. The workflow leading to a segmented image is not straightforward or unique and, for most of the properties of interest, a ground truth is not available. For this reason, it is crucial to understand how image processing choices control properties estimation. In this work, we assess the sensitivity of porosity, permeability, specific surface area, *in situ* contact angle measurements, fluid-fluid interfacial curvature measurements and mineral composition to processing choices. We compare the results obtained upon the employment of two processing pipelines: non-local means filtering followed by watershed segmentation; segmentation by a manually trained random forest classifier. Single-phase flow permeability,

Gaetano Garfi
Imperial College London, Department of Earth Science and Engineering, London, UK
E-mail: g.garfi17@imperial.ac.uk

Cédric M. John
Imperial College London, Department of Earth Science and Engineering, London, UK

Steffen Berg
Shell Global Solutions International B.V., Amsterdam, The Netherlands and Imperial College London, Department of Earth Sciences and Engineering, Department of Chemical Engineering, London, UK

Samuel Krevor
Imperial College London, Department of Earth Science and Engineering, London, UK

in situ contact angle measurements and mineral-to-pore total surface area are the most sensitive properties, as a result of the sensitivity to processing of the phase boundary identification task. Porosity, interfacial fluid-fluid curvature and specific mineral descriptors are robust to processing. The sensitivity of the property estimates increases with the complexity of its definition and its relationship to boundary shape.

Keywords X-ray imaging · image processing · contact angle · fluid-fluid curvature · mineralogy

Article highlights

- Advanced multiphase flow properties are sensitive to the choice of the X-ray CT image processing pipeline
- *In situ* contact angle measurement, total mineral-to-pore surface area and single-phase flow permeability are particularly sensitive
- The phase boundary identification task is the main source for disagreement between estimates

1 Introduction

The investigation of multiphase flow phenomena in permeable media is of key interest in several research fields including hydrocarbon recovery (Blunt, 2017), carbon sequestration (Krevor et al., 2015), catalyst design (Wu et al., 2005; Lee et al., 2008), fuel cells (Debe, 2012; Andersson et al., 2016) and battery efficiency improvement (Newman, 1995; Sikha et al., 2004). There has long been interest in mechanisms underlying physical and chemical processes happening at the smallest characteristic length scales controlling flow and transport, the pores and fluid-solid interfacial areas within a system. However, their understanding has been limited by difficulties in observing key fluid and transport properties at the small scales of interest, within the opaque porous media.

In this context, the development of laboratory-based X-ray micro computed tomography - X-ray μ-CT - has led to rapid advances (Wildenschild and Sheppard, 2013). In recent years, the use of X-ray μ-CT has been used in the characterisation of rock and fluid flow properties (Blunt et al., 2013; Bultreys et al., 2016a,b). This has extended beyond estimates of simple rock and single-phase flow properties - pore volume, single-phase flow permeability - to include rock mineral composition (Lai et al., 2015), capillary pressure from fluid interfacial curvature (Armstrong et al., 2012; Lin et al., 2018), and the wetting state from fluid interfacial curvature and *in situ* contact angle measurements (AlRatrout et al., 2018; Andrew et al., 2014; Scanziani et al., 2017; AlRatrout et al., 2017).

Imaging and image processing are central to the quality of these observations (Schlüter et al., 2014; Iassonov et al., 2009). Rocks are imaged while saturated or partially saturated by one or more fluids, e.g. air, water, oil,

CO_2. The 3D image is a map of greyscale values proportional to a linear attenuation coefficient codified as a floating point or an integer number in 16 bits, where the constitutive element is a voxel - three-dimensional pixel. Quantitative information is derived from the image by assigning a phase to each voxel through a classification procedure called image segmentation. The segmentation procedure is often preceded by filtering and artefact removal. The workflow consisting of reconstruction, artefact removal, filtering and segmentation constitute the image processing task. This is thus the task which defines and builds the 3D dataset on which measurements are performed and simulations are run.

The sensitivities of the measurement to the image processing depend on both the processing pipeline used and the observation of interest. The sensitivities have been evaluated for porosity, single-phase flow permeability and fluid-fluid interfacial curvature (Saxena et al., 2017; Leu et al., 2014; Armstrong et al., 2012). A leading challenge in evaluating image processing is the acquisition of an independent ground truth measurement of the property of interest for benchmarking. Laboratory measured porosity and permeability have been used. However, it is challenging to reconcile porosity estimates from μ-CT images with those that are experimentally determined by standard laboratory methods. There are a number of causes for this including the presence of subresolution porosity especially in carbonates or clay minerals (Sok et al., 2010; Andrew et al., 2013; Soulaine et al., 2016). Leu et al. (2014) have also found it difficult to match at the same time porosity and permeability laboratory measurements with estimates from μ-CT images. In general, transport property estimates have also been found sensitive to processing choices (Leu et al., 2014; Saxena et al., 2017). The challenge is accentuated for the observation of multiphase flow characteristics for which there are few or no practical independent measurements available other than X-ray CT. As a result it is key to understand these sensitivities to imaging, processing, and analysis protocols.

The aim of this work is to investigate the role of the image processing pipeline choice for the measurement of multiphase flow properties beyond simple binary segmentation of the rock medium and estimation of single-phase flow properties. Thus we evaluate the sensitivity of porosity and single-phase flow permeability to image processing as a benchmark. We subsequently focus our evaluation on specific surface area, local three-phase contact angles, mean fluid-fluid interfacial curvature, and mineral volume fraction on five rock samples with distinct pore structures. The analysis of most of these properties requires multiclass segmentation, more challenging than standard binary segmentation. We compared the results obtained from the employment of two processing pipelines. The more widely used pipeline consisted of the sequential use of non-local means filtering and watershed segmentation. The second pipeline consisted in a machine learning based segmentation tool that eliminates the need of a filtering step, Trainable WEKA Segmentation 3D (TWS).

Table 1 Example mineral composition (weight percentage) from XRD/XRF measurements of the five rock lithologies considered. For Bentheimer sandstone refer to Peksa et al. (2015). For Berea sandstone, Ketton limestone, Edwards limestone, Estaillades limestone refer to Lai et al. (2015).

	Bentheimer	Berea	Ketton	Edwards	Estaillades
Dol	0.26	0.2-0.4	0	45.4	0
Ank	0	0.7-1.3	0	0	0
Cal	0.15	1.3-2.9	98.3	47	99.6
Qtz	91.7	70.3-73.1	1.7	7.6	0.4
Or	4.86	13.1-12.6	0	0	0
Ab	0	1.0	0	0	0
An	0	1.5-1.7	0	0	0
Kln	2.5	1.6-2.1	0	0	0
Ill	0	1.7-2.4	0	0	0
Sme	0	1.9-2.3	0	0	0
Chm	0	0.7-1.0	0	0	0
Clc	0	0.3-0.5	0	0	0
Py	0.03	1.7-2.6	0	0	0

2 Data and Methods

2.1 Datasets

Five rock samples were considered in this study: Bentheimer sandstone, Berea sandstone, Ketton limestone, Edwards limestone, and Estaillades limestone. For reference, previously measured laboratory mineral compositions are reported in Tab. 1 from Lai et al. (2015) and Peksa et al. (2015). We imaged five cylindrical rock samples with diameters of 4 mm with an FEI Heliscan microCT. The source voltage and the tube current were 75 kV and 95 mA, respectively. The attenuated radiation was measured with a flat panel detector of 2800×2800 pixels. The 2D raw images acquired through a helical trajectory were then reconstructed employing an iterative back projection algorithm, provided by the instrument manufacturer. The voxel resolution obtained was $2.5\,\mu$m. The analysis of the role of image processing in estimating rock properties was performed on five subvolumes extracted from the tomograms of the five rocks. The analysis of the sensitivity of mineral topological characterization was only conducted on a subvolume extracted from the Berea sandstone because it was the only sample with significant mineralogical heterogeneity.

In order to evaluate the sensitivity of the estimates of contact angle and interfacial fluid-fluid curvature, a publicly available image of a trapped decane ganglion from Singh and Blunt (2018) was considered. The image was acquired during a drainage-waterflooding experiment in a water-wet Ketton limestone sample. Image voxel resolution was $2\,\mu$m. A detailed description of the dataset and the protocol of the experiment from which it was obtained is provided in Singh et al. (2017).

2.2 Image processing methods

2.2.1 Image processing pipeline 1: Non-local means filtering and watershed segmentation

The first image processing pipeline used makes use of a filter and segmentation combination that has been widely used in studies of porous rocks. Filtering options typically applied in imaging permeable media are reviewed in (Kaestner et al., 2008). While computationally cheap filters such as the median and Gaussian filters typically exhibit good performance in reducing white noise and greyscale value outliers, they weaken the contrast in the edges between phases. In order to preserve these edges, more sophisticated filtering algorithms have been developed, such as anisotropic diffusion or Bayesian information theoretic techniques (Wildenschild and Sheppard, 2013). Among the many alternatives, the non-local means filtering algorithm has proven to be able to suppress image noise without significantly altering the information content of phase boundaries of an image (Buades et al., 2005). As a consequence non-local means algorithms have been the preferred filtering choice in many studies in the context of digital rock technology (Singh et al., 2016; Alhammadi et al., 2017; Scanziani et al., 2018). For this reason, a non-local means algorithm was chosen as the filtering option of interest in this study. The weighting factor is called a similarity factor and in this work it was always set to 0.3.

The watershed algorithm was used for segmentation in this pipeline. This algorithm transforms the greyscale values of each pixel or voxel in a greyscale image into a magnitude, sometimes referred to as a height value (Beucher and Meyer, 1993). Boundaries and seeds of the phases to segment are identified as the regions where the gradient is at a maximum or a minimum. The labels for the phases then expand from previously identified seeds in a way analogous to water filling crevices in a flooding process. In this study, watershed segmentation was performed using Thermofisher Avizo Fire 9.5 software. Reviews of some of the algorithms can be found in (Iassonov et al., 2009). In the past algorithms based on a global thresholding principle - either manual or automatic - were the most widely used segmentation approaches. Iassonov et al. (2009) have found their performances inferior to algorithms accounting for spatially varying image information. Analogously, Schlüter et al. (2014) identified Bayesian Markov random field segmentation, watershed segmentation, and converging active countour segmentation to perform better in multiclass classification. As a consequence, in recent years, the favoured algorithms are those involving the use of spatially specific statistics such as the gradient in voxel greyscale intensity. However, most of these algorithms are biased by the requirement of subjective user inputs (Wildenschild and Sheppard, 2013). Leu et al. (2014) quantified the sensitivity to the user choice of input parameters of three segmentation algorithms, i.e. global thresholding, hysteresis thresholding, and watershed. The use of the latter led to the most robust estimates of porosity, permeability and capillary pressure values in Berea sandstone.

2.2.2 Image processing pipeline 2: Machine learning based segmentation

Recently, the research community has shown interest in testing machine learning algorithms to segment porous media CT images. Cortina-Januchs et al. (2011) employed three unsupervised clustering algorithms, K-means, Fuzzy-C-means and Self Organising Maps, to build the feature vector used to train an artificial neural network, which was eventually used to detect solid soil and pore space in CT images. Chauhan et al. (2016b) extended that approach to 3D greyscale values. Moreover, they compared the performances of seven machine learning algorithms (either unsupervised and supervised) to segment four μ-CT imaged samples, concluding that the use of K-means to guide the construction of the feature vector dataset for Least-square support vector machine led to the best results (Chauhan et al., 2016a). Berg et al. (2018) employed Trainable WEKA Segmentation (TWS) (Arganda-Carreras et al., 2017) and no filtering to segment an artificially generated 2D orthogonal image of a Bentheimer sandstone sample. This processing pipeline was found to be more accurate and more robust to image noise and artefacts when compared with more traditional pipelines involving the sequential use of a filtering and a segmentation algorithm. Results shown in Andrew (2018) are in agreement with those of Berg et al. (2018).

In this study, the Trainable WEKA Segmentation 3D (TWS) (Arganda-Carreras et al., 2017) plugin of the open-source image processing software ImageJ (available in its Fiji distribution) was employed. A fast random forest classifier - a recent variation of random decision forest algorithms (Ho, 1994; Breiman, 2001) - was chosen among the pool of options available. The training of the classifier is performed making use of the data manually labelled by the user, on the basis of the features selected. In this work, the features selected for the training and the classification tasks were the mean and variance of each voxel. Both of these features are defined over a cubic region defined in the neighbourhood of each voxel, within a distance - ranging from 1 to 8 voxels from the position of the central voxel considered. For each feature - either mean or variance - and for each length value, a new image was created, where each voxel value corresponded to the mean (or variance) calculated over the region of the image defined by the length considered. Since machine learning based segmentation has proven to be robust to image noise (Berg et al., 2018; Andrew, 2018), no filtering was used prior to segmentation.

2.3 Estimation of rock properties

Porosity, specific surface area and single-phase flow permeability were computed and compared for all the images considered. Porosity was computed as the ratio between the pore space and the bulk volume of the image. Specific surface area was defined as the interfacial area between the pore space and the rock matrix, divided by rock matrix volume. All the volume and area measurements were performed by employing the label analysis toolbox avail-

able in Thermofisher Avizo 9.5. Single-phase flow permeability was computed running direct numerical simulations through the connected pore space. A pressure drop of 1 Pa was imposed, considering two opposite faces of the cubic sample as inlet and outlet boundaries, respectively. A solver available in openFOAM was employed (Raeini et al., 2012).

To compare results computed from the images segmented using the two segmentation pipelines, we used the relative difference between two estimates of the same property in a dataset,

$$d_x = \frac{x_W - x_{TWS}}{x_W} \tag{1}$$

where x_W is the estimate of the pore space property x obtained by employing the watershed segmentation, and x_{TWS} is the estimate made by employing Trainable WEKA Segmentation 3D.

2.4 *In situ* contact angle and fluid-fluid interfacial curvature measurements

The greyscale image of the trapped decane ganglion in a Ketton limestone pore was segmented with the processing pipelines 1 and 2. In order to perform contact angle measurements, the three-phase contact line - between decane, brine, and rock walls - was identified by employing the Thermofisher Avizo Fire 9.5 label interface toolbox. We then employed the algorithm proposed by Scanziani et al. (2017) to automatically measure the contact angles formed by the two fluids sitting on the rock matrix, along that contact line. The parameters chosen in the algorithm were the same for both the segmented images analysed.

To compute fluid-fluid interfacial area mean curvature, the interfacial area between the two fluids was identified. In order to exclude from our analysis values of curvature measurements performed in regions of the fluid-fluid interface close to rock walls, we followed the approach suggested in Singh et al. (2016). A dilation of three voxels was performed on the rock matrix label. The dilated rock label image was used to mask the three-phase segmented image, to obtain a third image where only fluid labels were present. This final image was used to reconstruct the fluid-fluid interface surface by means of a marching cube algorithm implemented in Thermofisher Avizo Fire 9.5. The reconstructed surface was smoothed smoothing extent parameter equal to 3 - to correct for the effect of voxelisation of the actual interface shape. Local mean curvature measurements were eventually performed.

2.5 Mineral topological characterization

The sensitivity of the mineral characterization task was evaluated for a subsample of the Berea sandstone image. The analysis was performed on a 500^3 voxels cubic subvolume of the imaged sample, i.e. 1.95 mm^3.

In order to choose the minerals to be segmented in the image obtained by X-ray micro-CT, scanning electron microscopy (SEM) was employed to aid with mineral identification. A second specimen from the same core of the one imaged was used to create the SEM imagery. SEM operated in back scattered electron (BEC) mode coupled with energy dispersive X-ray spectroscopy (EDS) allowed for the identification of the main mineral groups present.

The 500^3 voxels greyscale image was thus processed with the two pipelines assessed in this work. The number of the phases to segment was chosen on the basis of the combined information obtained from SEM and X-ray micro-CT imagery. Through SEM the main mineral groups identified were: clay minerals, quartz, feldspar, calcite cementation and non-specified minerals embedding heavy metal compounds. On the basis of SEM + EDS results and previous work by Lai et al. (2015) we chose to segment the CT image into six phases: pore space, clay minerals, quartz, feldspar group minerals, calcite cementation and others highly attenuating minerals. On the other hand, a closer look to the grey scale image, revealed that only five of the six phases initially chosen showed clear differences in their average grey scale value. In particular, the grey scale values belonging to the grains reconcilable to quartz and feldspar minerals were very similar. Therefore, it was chosen to reduce the number of the phases to segment to five: pore space, clay minerals, quartz-feldspar minerals, calcite cementation and other highly attenuating minerals. Finally, two segmented images were obtained, one for each segmentation algorithm employed.

From the two segmented images, volume as well as mineral-to-pore surface areas were computed. The volume fractions were computed as the ratio between the total volume of each phase to the total bulk volume. Mineral-to-pore surface areas measured the total surface area that a certain mineral group shared with the pore space. The interfaces between each mineral phase and the pore space were thus identified and their area was computed by employing Thermofisher Avizo Fire 9.5 software. Finally, mineral-to-pore surface area fractions were computed as the ratio between each mineral-to-pore surface area and the total surface area shared by the pore space and the entire rock matrix. All the area and volume measurements were performed with the label analysis package available in Thermofisher Avizo Fire 9.5.

3 Results and Discussion

3.1 Sensitivity of porosity, specific surface area, and single-phase flow permeability

Fig. 1 shows the greyscale cross sections of the datasets considered for this analysis. For each rock, the figure also shows the differential image obtained by subtracting the WEKA segmented image from the watershed segmented image. Misclassified voxels are mainly concentrated in the boundary regions between the pore space and the rock matrix.

Table 2 Relative differences (d_x) of the estimates of porosity (ϕ) specific surface area (A_s) and single-phase flow permeability (K) obtained from images segmented with the two processing pipelines considered.

	$d_\phi[-]$	$d_{A_s}[-]$	$d_K[-]$
Bentheimer	0.026	0.047	0.145
Berea	0.256	0.165	0.829
Ketton	0.065	-0.108	0.343
Edwards	0.095	-0.262	0.684
Estaillades	-0.148	-0.148	-0.589

Fig. 2 reports the estimates of porosity, surface area, and permeability, while Table 2 shows the relative differences for each property and each sample. Porosity estimates show small differences for most of the samples considered. The smallest difference was observed for Bentheimer sandstone, while the largest was observed for the Berea sandstone. Trainable WEKA Segmentation 3D systematically overestimated the fraction of rock matrix compared to the watershed segmentation in all samples but Estaillades limestone.

Bentheimer sandstone showed the least variation in the estimates for specific surface area and the single-phase flow permeability. In contrast, the largest discrepancy in specific surface area was observed for Edwards limestone, while Berea sandstone shows the largest difference for estimates of single-phase flow permeability. This is consistent with the observed sensitivity for porosity.

The relative differences were larger for single-phase flow permeability than porosity and specific surface area. In attempt to identify the sources of such large sensitivities for estimates of permeability, a maximum ball extraction (Raeini et al., 2017) was performed on each segmented image, and pore size distributions were obtained. Although the shape of the distributions are similar, small shifts towards larger values of pore diameters were observed when permeability increased. Single-phase flow permeability estimates were found sensitive to these changes. These changes may thus strongly impact the overall connectivity of the pore space.

The observation that single-phase flow permeability relative differences are larger than those observed for porosity and surface area suggests that the sensitivity of an estimate to the image processing pipeline increases with the complexity of the interpretation. An analogous conclusion is suggested by the results obtained from the computation of contact angle and fluid-fluid interfacial curvature measurements.

3.2 Sensitivity of *in situ* contact angle and fluid-fluid interfacial curvature measurements

The three-phase contact lines identified in the two segmented images and their difference are shown in Fig. 3. There are significant differences between the segmentation pipelines, and contact angle measurements are unsurprisingly

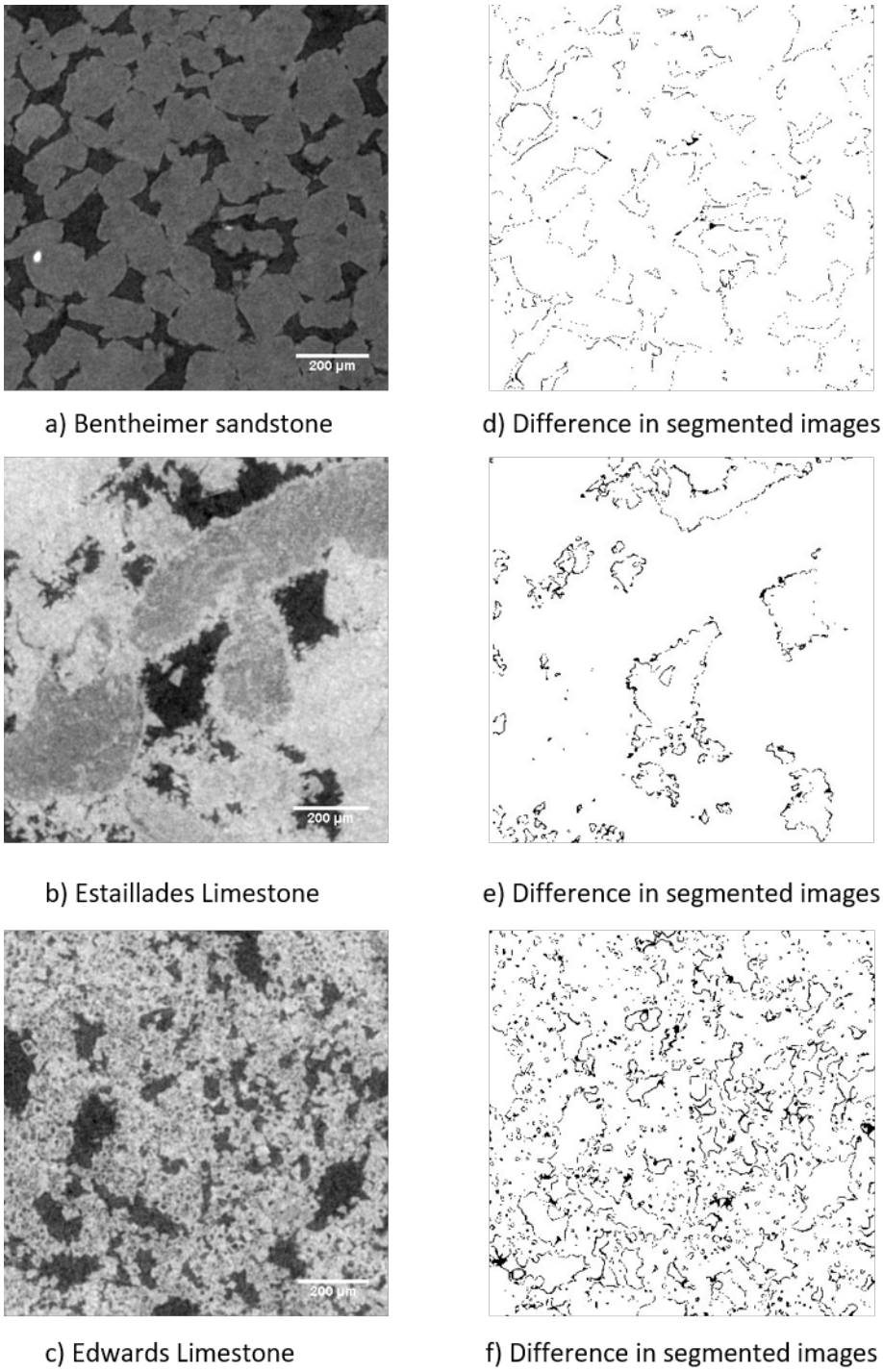

Fig. 1 Cross sections of three of the five samples considered for the analysis of pore space properties sensitivity to image processing. The voxel resolution is 2.5 μm. The rocks are, respectively: a) Bentheimer sandstone; b) Estaillades limestone; c) Edwards limestone and the differential images obtained by subtracting the respective segmented images with the two processing pipelines considered.

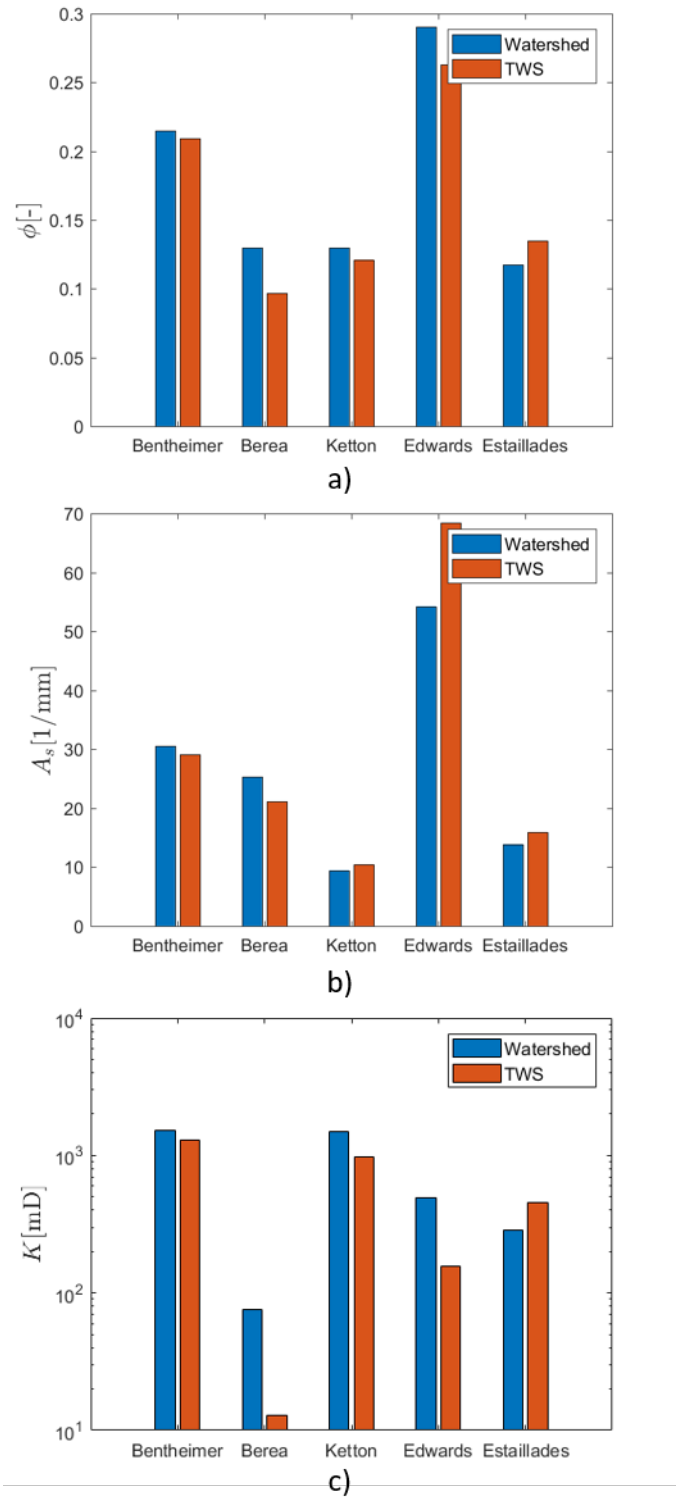

Fig. 2 Pore space properties estimates for the five rock samples considered: a) Porosity (ϕ [−]); b) Specific surface area (A_s [1/mm]); c) Single-phase flow permeability (K [mD]). Estimates are shown for both the segmentation approaches under investigation. The largest difference in estimates is observed for single-phase flow permeability.

dissimilar. The mean and standard deviation of the measurements obtained in the two cases are reported in Tab.3, while the discrete probability density functions for the contact angle measurements are reported in Fig.4. The difference in the the mean and standard deviation are 5.43° and 3.46°, respectively. Moreover, the large difference in the estimated skewness parameter for the two distributions (Tab.3) confirms that the two distributions are distinct.

The measurements we obtained on the watershed segmented image differ from those Scanziani et al. (2017) obtained on the very same dataset, because of the different similarity value chosen and the subjective choice of phase thresholds in applying watershed segmentation. Both studies underestimate the mean contact angle relative to those manually performed in Singh et al. (2016). On the other hand, the employment of the automatic algorithm on the TWS segmented image leads to a mean contact angle very similar to that measured in Singh et al. (2016), although measurements standard deviation is noticeably larger.

On the other hand, the differences observed for the measurements of fluid-fluid interfacial curvature are much smaller. The difference in the mean value is $0.3\,\mu\mathrm{m}^{-1}$, while the difference in standard deviation is $0.15\,\mu\mathrm{m}^{-1}$. The probability density functions associated with local mean curvature measurements - reported in Fig.4 - show agreement, as confirmed by the very small difference in their skewness parameter (Tab.3). Their shapes are similar, with a similar tailing of the distributions with increasing mean curvature.

The outcome of this analysis suggests that interfacial curvature measurement is less sensitive to the image processing workflow than the meausurement of contact angle. This is a result of fluid-fluid interfaces being defined over a larger number of voxels as opposed to the three-phase contact lines. Contact angles are measured close to the point where three different phases meet, so that partial volume effects and resolution limits are more important (Leu et al., 2014; Soulaine et al., 2016; Saxena et al., 2017). Moreover, additional complications in performing the measurement are added by the rock matrix boundaries, which are the regions of an image exhibiting the largest variability when segmented, due to various levels of resolvable and sub-resolution roughness (AlRatrout et al., 2018). By comparing the results obtained for contact angle measurements and fluid-fluid interfacial curvature we observe again that the sensitivity to the choice of the image processing pipeline increases with the complexity in the definition and interpretation of the quantity computed from the images.

3.3 Sensitivity of the rock mineralogy descriptors

The Berea sandstone tomogram was segmented into five phases: pore space, clay minerals, quartz-feldspar minerals, calcite cementation, others highly attenuating minerals (Fig.5). The volume renderings of each phase segmented is shown in Fig.6. They demonstrate the complexity of the topology of chemical heterogeneities in natural porous media.

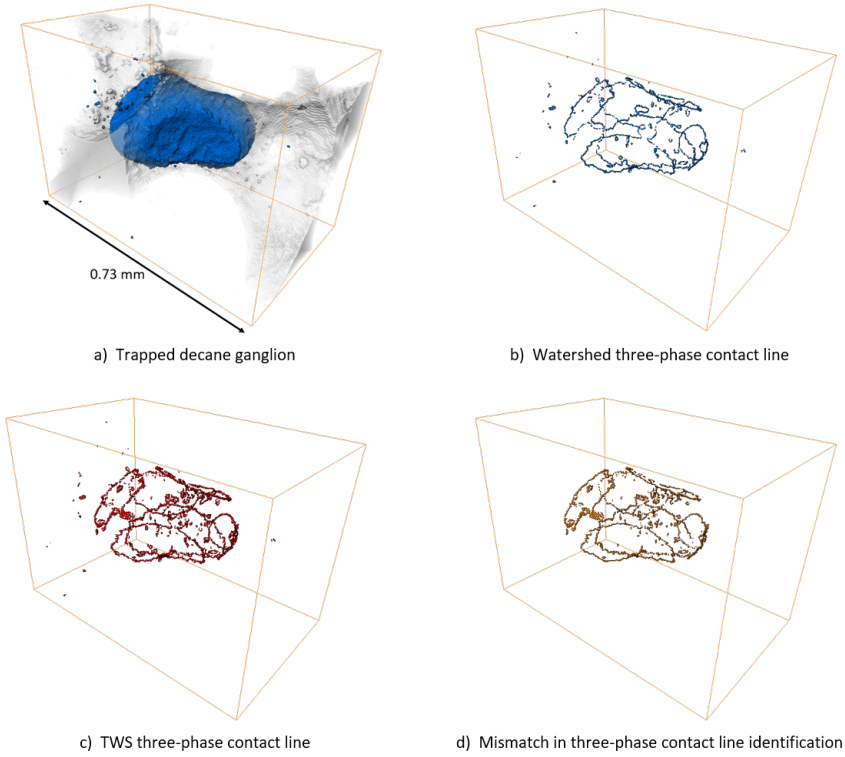

Fig. 3 Three-phase contact lines were identified in segmented images to measure contact angles: a) Volume rendering of the segmented trapped decane ganglion; b) Contact lines identified in the image processed by non-local means filtering and watershed segmentation; c) Contact line in the image processed by Trainable WEKA Segmentation 3D (TWS); d) Differential image of the two contact lines.

Table 3 Results of contact angle (θ) and fluid-fluid interfacial curvature (κ) measurement, computed on the same image segmented through two different image processing pipelines.

	Watershed	TWS	$d_x[-]$
Mean $\theta\,[°]$	41.873	47.301	-0.130
St.Dev $\theta\,[°]$	15.299	18.762	-0.226
Skewness $\theta\,[°]$	0.397	0.517	-0.302
Mean $\kappa\,[1/\mu m]$	0.455	0.494	-0.086
St.Dev $\kappa\,[1/\mu m]$	1.178	1.335	-0.133
Skewness $\kappa\,[1/\mu m]$	7.595	7.913	-0.042

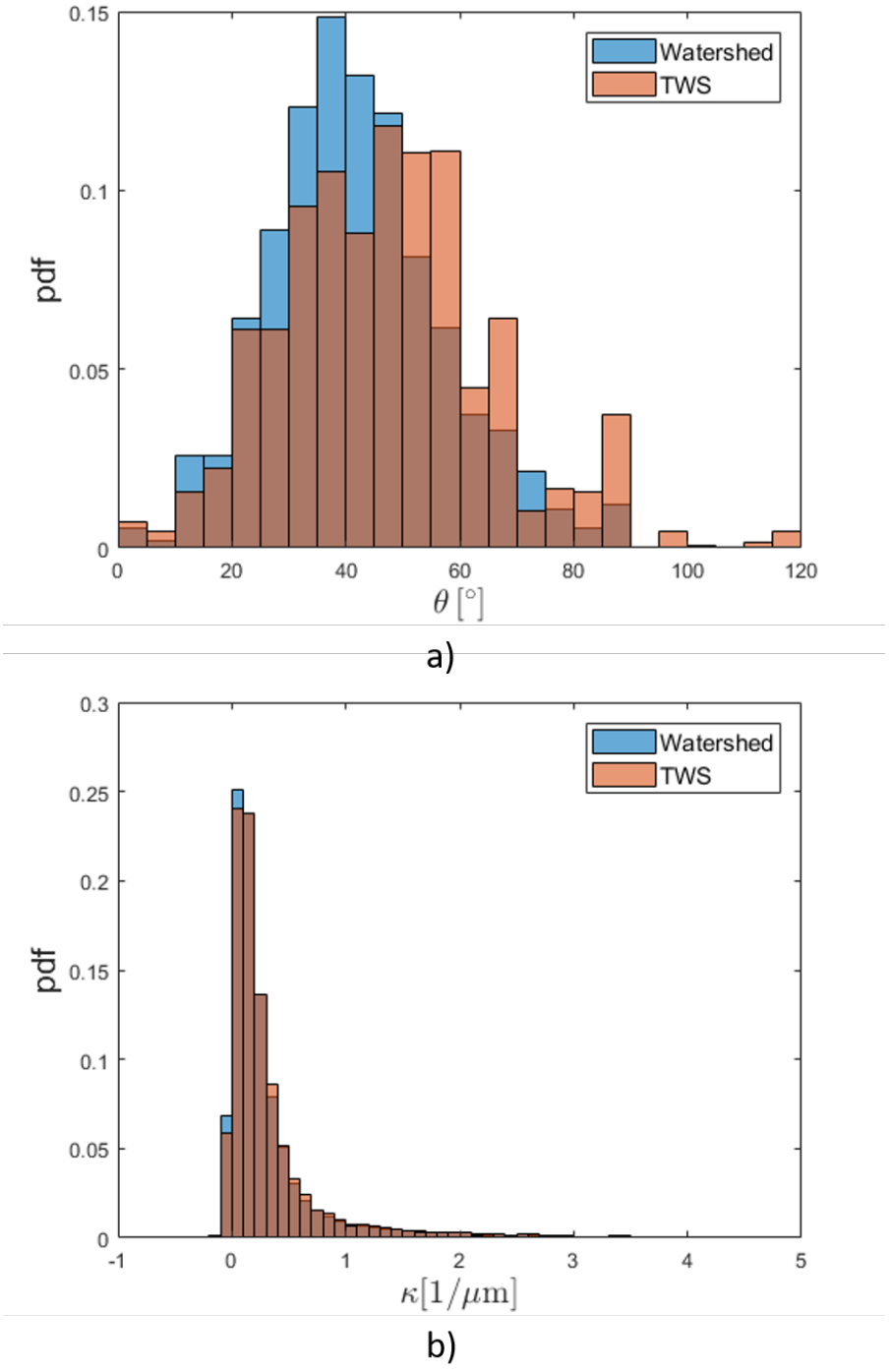

Fig. 4 Probability density functions associated with the measurements of contact angle θ [°] and fluid-fluid interfacial mean curvature κ [$1/\mu$m] from the same greyscale image segmented with watershed segmentation and Trainable WEKA Segmentation 3D (TWS).

Table 4 Volume fraction of each phase in the images segmented employing the two image processing pipelines under investigation. The volume fraction was defined as the ratio between the volume of each phase to the total volume in the image.

	Watershed [−]	TWS [−]	d_x
Pore	0.079	0.081	-0.031
Clay	0.038	0.039	-0.045
Quartz - Feldspar	0.771	0.746	0.032
Calcite	0.109	0.123	-0.134
Others	0.004	0.010	-1.405

Table 5 Surface area of the interface between each mineral and the pore space - mineral-to-pore surface area - calculated in the segmented images obtained with watershed and Trainable WEKA Segmentation 3D (TWS).

	Watershed [mm^2]	TWS [mm^2]	d_x
Clay	16.669	22.041	-0.322
Quartz - Feldspar	35.195	45.948	-0.306
Calcite	1.643	3.468	-1.111
Others	0.176	0.126	0.284

Tab.4 reports the results obtained for the computation of the volume fraction of each phase. The sensitivity of these quantities are small compared to what was observed for other quantities previously analysed in this study. Analogous results are observed for mineral-to-pore surface area fractions (Tab.6). On the other hand, a substantial difference is observed in the mineral-to-pore surface area estimates (Tab.5), with much larger interfaces between clay, quartz-feldspar and calcite cementation and the pore space in the image segmented by Trainable WEKA Segmentation 3D. This suggests that the interfaces identified by Trainable WEKA Segmentation 3D are much rougher than those identified by watershed algorithm. Such a large variation of the total exposed surface area may have significant implications in the context of reactive transport modelling.

This finding suggests once more that the sensitivity to image processing is larger when the property of interest is more complex to derive. The sensitivity to image processing seems to become more and more relevant when the definition of the property of interest is more closely related to phase boundary shape. Indeed, the same has already been observed for single-phase flow permeability, where boundary conditions and geometry contribute to the description of the interaction between solid walls and the fluid; the same has also been observed for contact angle measurement, which definition relies of the identification of the contact line between three different phases.

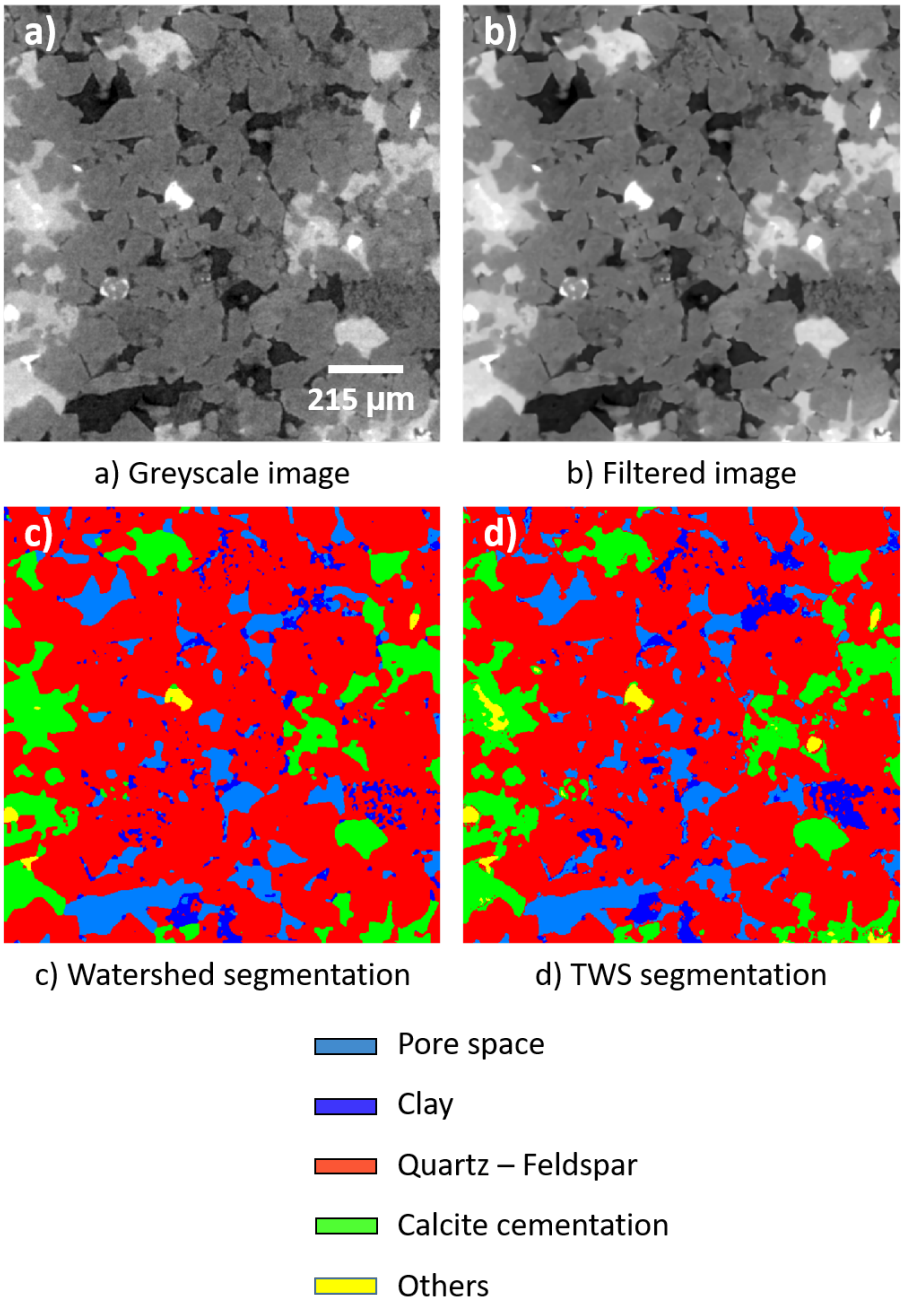

Fig. 5 Orthogonal slices of the 500 × 500 × 500 voxels CT image of a Berea sandstone. Watershed segmentation was performed on the non-local means filtered image, while TWS was employed on the greyscale unfiltered one.

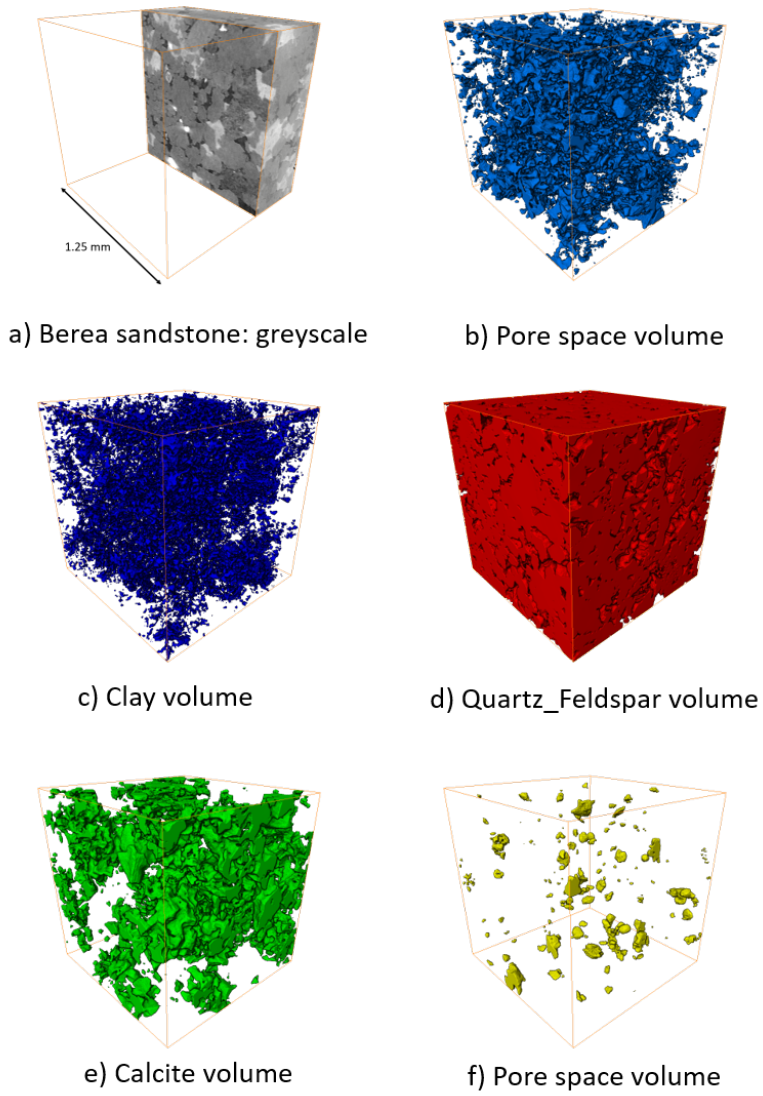

Fig. 6 Volume renderings of the $500 \times 500 \times 500$ voxels CT image of a Berea sandstone: greyscale image and segmented phases upon employment of non-local means filtering and watershed segmentation.

3.4 Wider implications

A broad assessment of the results suggests that the sensitivity of the properties of interest increases with the complexity of the interpretation of the observation, and also with the complexity of the rock structure. Porosity and mineral volume fractions were the properties affected the least by the choice of the

Table 6 Surface area fraction of the interface between each mineral and the pore space - mineral-to-pore surface area fraction - calculated in the segmented images obtained upon employment of the two image processing pipelines. Surface area fraction has been defined as the ratio between the surface area of the interface shared by each mineral and the pore space and the total surface area of the interface shared by the pore space with the whole rock matrix.

	Watershed [−]	TWS [−]	d_x
Clay	0.311	0.308	0.008
Quartz - Feldspar	0.656	0.642	0.021
Calcite	0.031	0.048	-0.583
Others	0.003	0.002	0.463

processing pipeline. We hypothesize that this is a consequence of their definitions: both definitions rely on calculations performed over larger regions of the images. This reduces the relative importance of phase boundary identification, a sensitive task of image processing. Analogously, we do not expect fluid saturation to be very sensitive to image processing. Conversely, if one considers the definition of the contact angle, it relies on the precise identification of both fluid-fluid and fluid-solid boundaries. Moreover, partial volume effects are significantly amplified by the requirement of a three-phase boundary. As a consequence, the combination of two potential sources of errors may lead to appreciably inconsistent measurements. In the same way, single-phase flow permeability estimation suffers from issues related to boundary identification. This is particularly relevant for rocks in which smaller throats constitute an important contribution to connectivity. Moreover, although we did not investigate the role of voxel resolution on image segmentation results, it is well known that it controls the estimation of petrophysical properties (Combaret et al., 2013a,b). Consequently, we expect quantities whose computation is strongly related to smaller features in the images - such as contact angle measurement and single-phase flow permeability - to be sensitive to voxel resolution as well.

4 Conclusions

We presented an assessment and a comparison of the quantitative results obtained from X-ray micro-CT images segmented using two different image processing approaches: non-local means filtering followed by watershed segmentation; machine learning based segmentation with a fast random forest classifier (Ho, 1994; Breiman, 2001). In order to assess the relative importance of the image processing pipeline selected, diverse datasets and properties to compute were considered. In particular, the focus of this work was to extend our understanding of sensitivity of image processing to the estimation of multiphase fluid properties (*in situ* contact angle, interfacial curvature) and mineral phase segmentation.

Porosity, specific surface area and single-phase flow permeability were estimated in ten two-phase (rock matrix and pore space) segmented images.

Single-phase flow permeability proved to be the most sensitive property to the processing pipeline chosen.

Contact angles and fluid-fluid interfacial curvature were measured in an image of a trapped decane ganglion in a water-wet Ketton limestone pore (Singh et al., 2016; Singh and Blunt, 2018). Contact angle measurements obtained with an automatic algorithm (Scanziani et al., 2017) on the machine learning segmented image reconciled well to those manually measured by (Singh et al., 2016). Measurements of contact angle, while comparable to past studies, were sensitive to image processing workflows. On the contrary, measurements of fluid-fluid interfacial curvature were insensitive to image processing workflows.

Four mineral groups and the pore space were segmented in a Berea sandstone. Estimates of mineral fractions as well as mineral-to-pore surface area fractions were insensitive to image processing workflows. The same was not true for mineral-to-pore surface area, which suggests that the choice of the processing pipeline may be particularly relevant for reactive transport modelling applications.

The greatest sensitivities in image processing arise in the identification of boundaries where partial volume and resolution effects may be significant. Sensitivity increases with increasing dependence on boundary identification and decreasing availability of the necessary boundaries in the image.

References

Alhammadi AM, AlRatrout A, Singh K, Bijeljic B, Blunt MJ (2017) In situ characterization of mixed-wettability in areservoir rock at subsurface conditions. Scientific Reports 7(1):10753, DOI 10.1038/s41598-017-10992-w

AlRatrout A, Raeini AQ, Bijeljic B, Blunt MJ (2017) Automatic measurement of contact angle in pore-space images. Advances in Water Resources 109:158–169, DOI 10.1016/j.advwatres.2017.07.018

AlRatrout A, Blunt MJ, Bijeljic B (2018) Wettability in complex porous materials, the mixed-wet state, and its relationship to surface roughness. Proceedings of the National Academy of Sciences 115(36):8901–8906, DOI 10.1073/pnas.1803734115

Andersson M, Beale SB, Espinoza M, Wu Z, Lehnert W (2016) A review of cell-scale multiphase flow modeling, including water management, in polymer electrolyte fuel cells. Applied Energy 180:757–778, DOI 10.1016/j.apenergy.2016.08.010

Andrew M (2018) A quantified study of segmentation techniques on synthetic geological XRM and FIB-SEM images. Computational Geosciences 22:1503, DOI 10.1007/s10596-018-9768-y

Andrew M, Bijeljic B, Blunt MJ (2013) Pore-scale imaging of geological carbon dioxide storage under in situ conditions. Geophysical Research Letters 40(15):3915–3918, DOI 10.1002/grl.50771

Andrew M, Bijeljic B, Blunt MJ (2014) Pore-scale contact angle measurements at reservoir conditions using X-ray microtomography. Advances in Water Resources 68:24–31, DOI 10.1016/j.advwatres.2014.02.014

Arganda-Carreras I, Kaynig V, Rueden C, Eliceiri KW, Schindelin J, Cardona A, Seung HS (2017) Trainable Weka Segmentation: A machine learning tool for microscopy pixel classification. Bioinformatics 33(15):2424–2426, DOI 10.1093/bioinformatics/btx180

Armstrong RT, Pentland CH, Berg S, Hummel J, Lichau D, Bernard L, Group VS (2012) Estimation of curvature from micro-CT liquid-liquid displacement studies with pore scale resolution pp 1–6

Berg S, Saxena N, Shaik M, Pradhan C (2018) Generation of ground truth images to validate micro-CT image-processing pipelines. The Leading Edge 37(6):412–420, DOI 10.1190/tle37060412.1

Beucher S, Meyer F (1993) The morphological approach to segmentation: the watershed transformation. Mathematical Morphology in Image Processing pp 433–481, DOI Export Date 6 May 2013

Blunt MJ (2017) Multiphase Flow in Permeable Media. Cambridge University Press, DOI 10.1017/9781316145098

Blunt MJ, Bijeljic B, Dong H, Gharbi O, Iglauer S, Mostaghimi P, Paluszny A, Pentland C (2013) Pore-scale imaging and modelling. Advances in Water Resources 51:197–216, DOI 10.1016/j.advwatres.2012.03.003

Breiman L (2001) Machine Learning. Kluwer Academic Publishers, DOI 10.1023/A:101093340

Buades A, Coll B, Morel J (2005) A non-local algorithm for image denoising. In: 2005 IEEE Computer Society Conference on Computer Vision and Pattern Recognition (CVPR'05), vol 2, pp 60–65 vol. 2, DOI 10.1109/CVPR.2005.38

Bultreys T, Boone MA, Boone MN, De Schryver T, Masschaele B, Van Hoorebeke L, Cnudde V (2016a) Fast laboratory-based micro-computed tomography for pore-scale research: Illustrative experiments and perspectives on the future. Advances in Water Resources 95:341–351, DOI 10.1016/j.advwatres.2015.05.012

Bultreys T, De Boever W, Cnudde V (2016b) Imaging and image-based fluid transport modeling at the pore scale in geological materials: A practical introduction to the current state-of-the-art. Earth-Science Reviews 155:93–128, DOI 10.1016/j.earscirev.2016.02.001, 1209.3974

Chauhan S, Rühaak W, Anbergen H, Kabdenov A, Freise M, Wille T, Sass I (2016a) Phase segmentation of X-ray computer tomography rock images using machine learning techniques: An accuracy and performance study. Solid Earth 7(4):1125–1139, DOI 10.5194/se-7-1125-2016

Chauhan S, Rühaak W, Khan F, Enzmann F, Mielke P, Kersten M, Sass I (2016b) Processing of rock core microtomography images: Using seven different machine learning algorithms. Computers and Geosciences 86:120–128, DOI 10.1016/j.cageo.2015.10.013

Combaret N, Dvorkin J, Glatt E, Han J, Kabel M, Keehm Y, Krzikalla F, Lee M, Madonna C, Marsh M, Mukerji T, Saenger EH, Sain R, Saxena N,

Ricker S, Wiegmann A, Zhan X (2013a) Computers & Geosciences Digital rock physics benchmarks Part I : Imaging and segmentation 50:25–32, DOI 10.1016/j.cageo.2012.09.005

Combaret N, Dvorkin J, Glatt E, Han J, Kabel M, Keehm Y, Krzikalla F, Lee M, Madonna C, Marsh M, Mukerji T, Saenger EH, Sain R, Saxena N, Ricker S, Wiegmann A, Zhan X (2013b) Computers & Geosciences Digital rock physics benchmarks part II : Computing effective properties 50:33–43, DOI 10.1016/j.cageo.2012.09.008

Cortina-Januchs MG, Quintanilla-Dominguez J, Vega-Corona A, Tarquis AM, Andina D (2011) Detection of pore space in CT soil images using artificial neural networks. Biogeosciences 8(2):279–288, DOI 10.5194/bg-8-279-2011

Debe MK (2012) Electrocatalyst approaches and challenges for automotive fuel cells. Nature 486(7401):43–51, DOI 10.1038/nature11115

Ho TK (1994) Random decision forests. Proceedings of 3rd International Conference on Document Analysis and Recognition 1:278–282, DOI 10.1109/ICDAR.1995.598994

Iassonov P, Gebrenegus T, Tuller M (2009) Segmentation of X-ray computed tomography images of porous materials : A crucial step for characterization and quantitative analysis of pore structures. Water Resources Research 45:1–12, DOI 10.1029/2009WR008087

Kaestner A, Lehmann E, Stampanoni M (2008) Imaging and image processing in porous media research. Advances in Water Resources 31(9):1174–1187, DOI https://doi.org/10.1016/j.advwatres.2008.01.022

Krevor S, Blunt MJ, Benson SM, Pentland CH, Reynolds C, Al-menhali A, Niu B (2015) International Journal of Greenhouse Gas Control Capillary trapping for geologic carbon dioxide storage From pore scale physics to field scale implications. International Journal of Greenhouse Gas Control 40:221–237, DOI 10.1016/j.ijggc.2015.04.006

Lai P, Moulton K, Krevor S (2015) Pore-scale heterogeneity in the mineral distribution and reactive surface area of porous rocks. Chemical Geology 411(0):260–273, DOI 10.1016/j.chemgeo.2015.07.010

Lee J, Park JC, Bang JU, Song H (2008) Precise Tuning of Porosity and Surface Functionality in Au @ SiO 2 Nanoreactors for High Catalytic Efficiency. Chemistry of Materials 20(18):5839–5844, DOI 10.1021/cm801149w

Leu L, Berg S, Enzmann F, Armstrong RT, Kersten M (2014) Fast X-ray Micro-Tomography of Multiphase Flow in Berea Sandstone: A Sensitivity Study on Image Processing. Transport in Porous Media 105(2):451–469, DOI 10.1007/s11242-014-0378-4

Lin Q, Bijeljic B, Pini R, Blunt MJ, Krevor S (2018) Imaging and Measurement of Pore-Scale Interfacial Curvature to Determine Capillary Pressure Simultaneously With Relative Permeability. Water Resources Research 54(9):7046–7060, DOI 10.1029/2018WR023214

Newman J (1995) Optimization of Porosity and Thickness of a Battery Electrode by Means of a Reaction-Zone Model. Journal of the Electrochemical Society 142(1):97–101

Peksa AE, Wolf KHA, Zitha PL (2015) Bentheimer sandstone revisited for experimental purposes. Marine and Petroleum Geology 67:701–719, DOI 10.1016/j.marpetgeo.2015.06.001

Raeini AQ, Blunt MJ, Bijeljic B (2012) Modelling two-phase flow in porous media at the pore scale using the volume-of-fluid method. Journal of Computational Physics 231(17):5653–5668, DOI 10.1016/j.jcp.2012.04.011

Raeini AQ, Bijeljic B, Blunt MJ (2017) Generalized network modeling : Network extraction as a coarse-scale discretization of the void space of porous media. Physical Review E 96(1):1–17, DOI 10.1103/PhysRevE.96.013312

Saxena N, Hofmann R, Alpak FO, Dietderich J, Hunter S, Day-stirrat RJ (2017) Effect of image segmentation & voxel size on micro-CT computed effective transport & elastic properties. Marine and Petroleum Geology 86:972–990, DOI 10.1016/j.marpetgeo.2017.07.004

Scanziani A, Singh K, Blunt MJ, Guadagnini A (2017) Automatic method for estimation of in situ effective contact angle from X-ray micro tomography images of two-phase flow in porous media. Journal of Colloid and Interface Science 496:51–59, DOI 10.1016/j.jcis.2017.02.005

Scanziani A, Singh K, Bultreys T, Bijeljic B, Blunt MJ (2018) In situ characterization of immiscible three-phase flow at the pore scale for a water-wet carbonate rock. Advances in Water Resources 121:446–455, DOI 10.1016/j.advwatres.2018.09.010

Schlüter S, Sheppard A, Brown K, Wildenschild D (2014) Image processing of multiphase images obtained via X-ray microtomography: A review. Water Resources Research 50(4):3615–3639, DOI 10.1002/2014WR015256

Sikha G, Popov BN, White RE (2004) Effect of Porosity on the Capacity Fade of a Lithium-Ion Battery. Journal of The Electrochemical Society pp 1104–1114, DOI 10.1149/1.1759972

Singh K, Blunt M (2018) High resolution x-ray micro-tomography datasets for in-situ effective contact angle analysis in carbonate rocks. http://www.digitalrocksportal.org/projects/125, DOI 10.17612/P7D95F

Singh K, Bijeljic B, Blunt M (2016) Imaging of oil layers, curvature, and contact angle in a mixed-wet and a water-wet carbonate rock. Water Resources Research 52:1716–1728, DOI 10.1002/2015WR018072

Singh K, Scholl H, Brinkmann M, Michiel MD, Scheel M, Herminghaus S, Seemann R (2017) The Role of Local Instabilities in Fluid Invasion into Permeable Media. Scientific Reports 7(1):1–11, DOI 10.1038/s41598-017-00191-y

Sok R, Varslot T, Ghous A, Latham S, P Sheppard A, A Knackstedt M (2010) Pore scale characterization of carbonates at multiple scales: Integration of micro-CT, BSEM, and FIBSEM. Petrophysics 51

Soulaine C, Gjetvaj F, Garing C, Roman S, Russian A, Gouze P, Tchelepi HA (2016) The Impact of Sub-Resolution Porosity of X-ray Microtomography Images on the Permeability. Transport in Porous Media 113(1), DOI 10.1007/s11242-016-0690-2

Wildenschild D, Sheppard AP (2013) X-ray imaging and analysis techniques for quantifying pore-scale structure and processes in subsurface

porous medium systems. Advances in Water Resources 51:217–246, DOI 10.1016/j.advwatres.2012.07.018

Wu CD, Hu A, Zhang L, Lin W (2005) A homochiral porous metal-organic framework for highly enantioselective heterogeneous asymmetric catalysis. Journal of the American Chemical Society 127(25):8940–8941, DOI 10.1021/ja052431t